



Cite this: *J. Mater. Chem. A*, 2024, **12**, 28882

Structural insights to metal ion linked multilayers on metal oxide surfaces *via* energy transfer and polarized ATR measurements†

Ashley Arcidiacono,^a Cory Ruchlin, ^b Grace M. McLeod, ^a Dhruba Pattadar,^c Sarah Lindbom,^a Alex J. Robb,^a Suliman Ayad,^a Nikolas R. Dos Santos,^a Igor V. Alabugin, ^a S. Scott Saavedra ^c and Kenneth Hanson ^{a*}

Metal ion linked multilayers offer a means of controlling interfacial energy and electron transfer for a range of applications including solar energy conversion, catalysis, sensing, and more. Despite the importance of structure to these interlayer transfer processes, little is known about the distance and orientation between the molecules/surface of these multilayer films. Here we gain structural insights into these assemblies using a combination of UV-Vis polarized visible attenuated total reflectance (p-ATR) and Förster Resonance Energy Transfer (FRET) measurements. The bilayer of interest is composed of a metal oxide surface, phosphonated anthracene molecule, Zn(II) linking ion, and a platinum porphyrin with one (P1), two (P2), or three (P3) phenylene spacers between the chromophoric core and the metal ion binding carboxylate group. As observed by both time-resolved emission and transient absorption, the FRET rate and efficiency decreases with an increasing number of phenylene spacers (P1 > P2 > P3). However, from p-ATR measurements we observe a change in orientation of porphyrins in the bilayer, which inhibits a uniform determination of the orientation factor (κ^2) across the series. Instead, we narrow the scope of viable structures by determining the best agreement between experimental and calculated FRET efficiencies. Additionally, we provide evidence that suggests, for the first time, that the bilayer structure is similar on both planar and mesoporous substrates.

Received 24th July 2024

Accepted 25th September 2024

DOI: 10.1039/d4ta05156d

rsc.li/materials-a

Introduction

The assembly of multiple molecular components at a metal oxide surface is of interest for their application in solar energy conversion, photocatalysis, sensing and more.^{1–3} Of the strategies for combining molecules at an interface (*e.g.*, electrostatics, co-deposition, covalent dyads, *etc.*),⁴ metal ion linked multilayers are appealing because (1) they are generated *via* a simple step-wise soaking procedure, (2) they avoid the synthetic complexities of covalently-bound dyads, (3) the components are modular, and (4) they circumvent the surface area limitation of co-deposited films.³ The strategic selection of components (*e.g.*, chromophores, catalysts, electron donors and/or acceptors, *etc.*) and their proximity to the surface can be used to facilitate directional energy and electron transfer as desired for their

application in photon upconversion,^{5–7} solar energy conversion,⁸ photocatalysis,^{9–11} molecular rectifying interfaces,^{12–15} and electrochromism.¹⁶

The rate and efficiency of these interfacial energy and electron transfer events are not only dependent on the energetics of the components but also the structure of the assembly (*i.e.*, the distance and orientation between the molecules/surface). In terms of structural insights into metal ion linked multilayers, the molecular and metal ion ratios have been quantified using UV-Vis spectroscopy, XPS, and mass spectrometry.^{3,17,18} Metal ion coordination and multilayer thickness have been determined from IR spectroscopy, atomic force microscopy, ellipsometry, X-ray photoelectron spectroscopy, and UV-Vis spectroscopy.^{3,19–22}

Recently, our team was the first to use polarized UV-Vis attenuated total reflectance (p-ATR) spectroscopy to determine the transition dipole moment orientation of each molecular layer²³ in metal ion linked bilayer²⁴ and trilayer films.²⁵ While p-ATR, and other grazing angle techniques (*e.g.*, XRR, IRRAS, *etc.*),^{26–28} lend some insight into the structure at molecule-metal oxide interfaces, they suffer from two fundamental limitations relevant to the materials discussed here. First, these measurements are performed on planar surfaces which may or may not accurately represent the structure on mesoporous substrates.²⁹

^aDepartment of Chemistry and Biochemistry, Florida State University, Tallahassee, Florida 32306, USA. E-mail: hanson@chem.fsu.edu

^bDepartment of Chemistry, McGill University, 801 Sherbrooke Street West, Montreal, Quebec, H3A 0B8, Canada

^cDepartment of Chemistry and Biochemistry, University of Arizona, Tucson, Arizona, 85721, USA

† Electronic supplementary information (ESI) available. See DOI: <https://doi.org/10.1039/d4ta05156d>



Second, they can only provide information about the molecular orientation relative to the substrate.^{30,31} The later issue is particularly problematic for multimolecular systems because, in the absence of an additional frame of reference (*i.e.*, the azimuthal angle), they cannot provide the orientation of the molecules relative to each other.²⁵

In this manuscript we describe our effort to address these shortcomings by using p-ATR in conjunction with Förster Resonance Energy Transfer (FRET) measurements to determine the structure of a metal ion-linked bilayer assembly. The bilayer of interest is shown in Fig. 1 and is composed of a mesoporous zirconium oxide substrate (ZrO_2), phosphonated anthracene molecule (**A**), Zn(II) linking ion, and a carboxylated, unsymmetrical porphyrin (**PX**, where $X =$ the number of phenylene spacers, 1, 2, or 3).

This bilayer ($\text{ZrO}_2\text{-A-Zn-PX}$) was chosen because it is a derivative of our previously studied molecular photon upconversion films,^{5,24,32,33} and it has appropriate energetics for ${}^3\text{PX}^*$ to A triplet energy transfer (TET) and ${}^1\text{A}^*$ to **PX** FRET.³² The latter energy transfer process, FRET, is particularly important here as it has well-known distance and orientation dependences as described in eqn (1) and (2).^{34–36}

$$E = \frac{1}{1 + \left(\frac{r_{\text{DA}}}{R_0}\right)^6} \quad (1)$$

$$R_0 = 9780(\kappa^2 \Phi_{\text{D}} n^{-4} J)^{1/6} \quad (2)$$

where E is the FRET efficiency, r_{DA} is the separation between donor and acceptor, R_0 is the Förster radius, J is the spectral overlap integral, n is the refractive index, Φ_{D} is the fluorescence quantum yield of the donor, and κ^2 is the orientation factor.

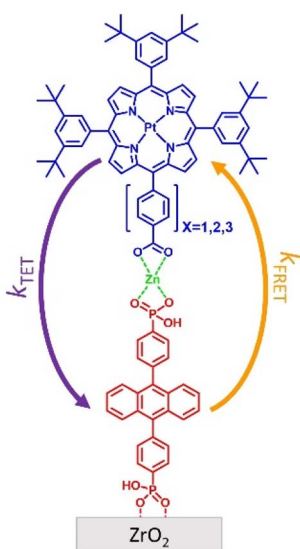


Fig. 1 General depiction of a metal ion linked bilayer composed of a ZrO_2 substrate, **A** (red), Zn(II) linking ion (green), and **PX** (blue) where X is the number of phenylene spacers. The directionality and rate constant for TET and FRET are depicted in purple and orange, respectively.

$$\kappa^2 = (\cos \alpha - 3 \cos \beta \cos \gamma)^2 \quad (3)$$

The orientation factor, κ^2 , is dependent on the angle between donor dipole moment and the intermolecular radial vector (α), acceptor dipole moment and radial vector (β), and donor and acceptor dipole moments (γ).

For a fixed pair of chromophores where J , n , and Φ_{D} are constant, then the relationship between measured values of E with respect to systematic variation in r_{DA} (*i.e.*, $n = 1\text{--}3$ in Fig. 1) could be used to determine κ^2 and, by extension, the relative orientation of the molecules in the bilayer film.^{37,38} That, in conjunction with p-ATR measurements (*i.e.*, the orientation relative to the surface), could provide a unique average geometry of the bilayer film.

Below, we recount our efforts using time-resolved emission and transient absorption to quantify the energy transfer rates and yields in the bilayer film depicted in Fig. 1. p-ATR is then used to determine the orientation of the chromophores relative to the surface. Due to orientation changes among **P1**, **P2**, and **P3** and the added complexity of the degenerate coplanar transition dipoles of **PX**, we were unable to determine a unique structure. Instead, we used calculated and experimental FRET efficiencies to narrow the scope of possible structures.

Experimental

Materials

Zinc acetate, boron trifluoride diethyl etherate, chloroform, benzonitrile, potassium hydroxide, methanol, dichloromethane, hexanes, and acetonitrile were purchased from Sigma-Aldrich and used without any further purification. 3,5-Di-*tert*-butylbenzaldehyde was purchased from Sigma-Aldrich and recrystallized from ethanol three times prior to use. 2,3-Dichloro-5,6-dicyano-*p*-benzoquinone (DDQ) and methyl 4-formyl benzoate were purchased from Alfa Aesar and used without further purification. Pyrrole was purchased from Sigma-Aldrich and distilled over calcium hydride (Sigma-Aldrich) prior to use. Benzonitrile was purchased from Sigma-Aldrich and distilled prior to use. Melatonix film and Vac'n Fill syringes were purchased from Solaronix. Glass substrates were acquired from Hartford Glass Co. Micro glass cover slides (18×18 mm) were obtained from VWR. ZrO_2 solgel pastes were prepared following previously reported procedures.³⁹ **A**⁴⁰ and **P3** (ref. 41) were synthesized following previously reported procedure. Synthetic details for **P1** and **P2** can be found in ESI.†

Film loading

Mesoporous ZrO_2 on glass substrates was functionalized with monolayers of **A** *via* soaking in a loading solution of $200 \mu\text{M}$ **A** in DMSO for 48 h. For the coordination of Zn(II), films were then submerged in a solution of $\text{Zn}(\text{CH}_3\text{COO})_2$ in MeOH ($500 \mu\text{M}$) for 2 h, followed by $150 \mu\text{M}$ **P1/P2** or 9.0 mg in 60 mL of **P3** in 1 : 1 chloroform : methanol until an **A** : **PX** ratio of $\sim 10 : 1$ was reached (15 minutes for **P1/P2** and 3 h for **P3**), resulting in $\text{ZrO}_2\text{-A-Zn-PX}$. Surface coverage isotherms can be found in ESI.† Films on planar ITO were loaded *via* a liquid flow cell



using the conditions listed in Table S5.† The adsorption isotherms (obtained with transverse magnetic polarized light) can be found in ESI.†

Absorption spectroscopy

Absorption spectra were acquired using an Agilent 8453 UV-visible photo diode array spectrophotometer. Thin film absorption spectra were collected *via* placing functionalized metal oxide films perpendicular to the detection path.

Steady-state and time-resolved emission

An Edinburgh FLS980 fluorescence spectrometer was used to obtain emission spectra. A 450 W Xe lamp coupled with a single grating (1800 1 mm⁻¹, 250 nm blaze) Czerny–Turner monochromator was used as output to excite the samples. Sample emission was passed through a 435 nm long pass filter then a single grating (1800 1 mm⁻¹, 500 nm blaze) Czerny–Turner monochromator and then detected by a Peltier-cooled Hamamatsu R928 photomultiplier tube. Time-resolved emission was collected at room temperature using the same Edinburgh FLS980 fluorescence spectrometer. Emission decay kinetics were obtained using multichannel scaling (MCS; >1 µs) or time-correlated single photon counting (TCSPC; <1 µs) with data collection until 10 000 counts. MCS measurements utilized excitation output from a 60 W microsecond flashlamp (pulse width <2.5 µs) at a 100 Hz repetition rate passed through a single grating (1800 1 mm⁻¹, 250 nm blaze) Czerny–Turner monochromator. Excitation for TCSPC was generated by an Edinburgh EPL-360 ps pulsed light emitting diode (360 ± 10 nm, pulse width 890 ps) with emission then passed through a single grating (1800 1 mm⁻¹, 500 nm blaze) Czerny–Turner monochromator and detected by a Peltier-cooled Hamamatsu R928 photomultiplier tube. For kinetics on films, a biexponential fitting using an IRF deconvolution²⁴ was used and a weighted average lifetime is reported.

Transient absorption

Transient absorption measurements were obtained using a HELIOS Fire transient absorption spectrometer (Ultrafast Systems). The spectrometer was coupled to the output of a Vitara-S Coherent Ti:sapphire laser amplifier using a 1 kHz Coherent Revolution-50 pump laser (5 mJ pulse, 150 fs fwhm at 800 nm). This output was split into a pump and probe beam. The probe was passed through a delay stage while the pump traveled through an optical parametric amplifier (OPerA Solo from Coherent) for wavelength selection. A white light supercontinuum, used for the probe, was produced by a sapphire crystal. The pump and probe beam were then overlapped on the sealed, deaerated sample that was mounted in a rastering stage. Difference spectra and single wavelength kinetics were collected averaging 3 times and holding for 3 seconds, with an exponential point acquisition beginning with 0.01 ps steps and totalling to 250 points. Chirp correction was processed using the Surface Xplorer software package from Ultrafast Systems.

Polarized visible attenuated total reflectance (p-ATR)

ATR spectroscopy measurements were conducted using a spectrometer described previously.⁴² ITO-coated glass slides (Thin Film Devices) served as planar waveguides. A Xe lamp (polarized and collimated) was coupled into and out of the waveguide using two BK7 ($n = 1.51$) prisms. The outcoupled light was directed into a monochromator (Newport MS260i) using a fiber-optic cable and was detected by a CCD camera (Andor iDus420A). The mean tilt angles of the absorbance dipoles of **A** in monolayer films and **A** and porphyrins in bilayer films were determined using previously described methods.³¹

Atomic layer deposition (ALD)

Glass microscope cover slides (VWR) were first sonicated in an HCl/ethanol (15/85% mix) solution for 20 minutes and then ethanol for 20 min. The glass was then dried under a stream of air. Atomic layer deposition (ALD) was performed using a Fiji G2 plasma enhanced atomic layer deposition system (Veeco). Tetrakis(dimethylamido)zirconium (TDMAZ) was purchased (STREM Chemical) as a precursor for deposition. Recipe for O₂ plasma deposition was obtained from the manufacturer and performed without modification. Briefly, the instrument heaters controlling the reactor, chuck, and delivery lines were set to 250 °C and the precursor was heated to 75 °C. The samples were then placed into the instrument platter, sealed inside the chuck, and the chuck and reactor were then pumped down from ambient pressure to vacuum (1×10^{-6} torr). Once under vacuum, the sample platter was then transferred to the reactor to begin the ALD process. Once in the reactor, the recipe pulsed the precursor at 30 sccm for 0.25 seconds, held for 5 seconds, applied 300 watts of plasma for 6 seconds, held for 5 seconds, and then repeated this process until the predetermined number of cycles was performed (40 cycles, ~1 Å per cycle) to generate a ~4 nm planar ZrO₂ film.

Results and discussion

Synthesis and surface loading

The molecules of interest for this study are shown in Fig. 1. Phosphonated anthracene derivative **A** was chosen as the FRET donor because it has a relatively high emission quantum yield ($\Phi_{ZrO_2, A} = 0.53$),⁴⁰ and its transition dipole moment is known to be aligned with the long axis of the molecule (*i.e.*, across the 9,10 carbon atoms of anthracene).⁴³ Furthermore, its properties at the interface have been extensively investigated in our lab.^{32,40,44}

As noted above, and in the molecular photon upconversion literature,^{7,45} Pt(II) porphyrin molecules make a well-known TET and FRET pair with anthracene derivatives. In contrast to our previously studied Pt(II) 5,10,15,20-(tetra-4-carboxyphenyl) porphyrin containing bilayers,^{32,46} the unsymmetric **P1-3** derivatives were designed to have only one carboxyl group (*i.e.*, a single Zn(II) coordination site) and the distance from **A** was systematically increased *via* the addition of phenylene spacing groups. **P1-3** were prepared using modification of previously published procedures with details provided in the ESI.†^{41,47,48}



P1–3 exhibit nearly identical Soret (400 nm) and Q-band (512 nm) features (Fig. S1†) indicating that the number of phenylene groups had minimal impact on ground state absorption of the porphyrin core. Similarly, the extinction coefficient and peak ratios of **P1–3** were comparable to that of symmetric Pt(n) porphyrins,³² suggesting that differences in meso-phenyl substitution did not introduce asymmetry to the porphyrins' degenerate transitions.⁴⁹

The bilayer film was assembled on mesoporous ZrO_2 . ZrO_2 was chosen due to its relatively high conduction band potential, inhibiting excited state electron transfer from **A** or **PX**.⁵⁰ Consequently, the photophysical properties of the assembly can be studied without concern of excited state quenching *via* interfacial electron transfer.³²

Metal ion-linked multilayers were assembled using a step-wise soaking procedure. ZrO_2 films were first soaked in a 300 μM DMSO solution of **A** for 24 hours and then a 500 μM methanol solution of $\text{Zn}(\text{OAc})_2$ for 2 hours. $\text{ZrO}_2\text{-A-Zn}$ films were then soaked in a 150 μM solution of **P1** or **P2** in chloroform:methanol (1 : 1, v/v) for 2 hours resulting in the $\text{ZrO}_2\text{-A-Zn-PX}$ bilayers. The loading isotherms for **P1** and **P2** on $\text{ZrO}_2\text{-A-Zn}$ are provided in the ESI (Fig. S4 and 5).[†] **P3** exhibited notably lower solubility than that of **P1** and **P2**. Consequently, $\text{ZrO}_2\text{-A-Zn-P3}$ bilayer films were prepared by soaking $\text{ZrO}_2\text{-A-Zn}$ in a saturated solution (9 mg in 60 mL) of **P3** in chloroform:methanol (1 : 1, v/v). A maximum surface loading of **P3** was achieved in 3 hours which, based on the UV-Vis spectra, resulted in an $\sim 10 : 1$ ratio for **A** : **P3**. For all subsequent measurements, the $\text{ZrO}_2\text{-A-Zn-P1}$ and $\text{ZrO}_2\text{-A-Zn-P2}$ films were prepared at the same 10 : 1 **A** : **PX** ratio to minimize any possible impact of chromophore ratios on excited state dynamics.

The absorption spectra of $\text{ZrO}_2\text{-A-Zn-P1}$ and its components are shown in Fig. 2 with spectra for all bilayer films provided in Fig. S6.[†] Consistent with previous reports, the bilayer film exhibits the additive features of its components indicating minimal direct coupling between the **A** and **PX** chromophores. Also highlighted are the 360 nm and 512 nm excitation wavelengths for selective excitation of **A** and **PX**, respectively.

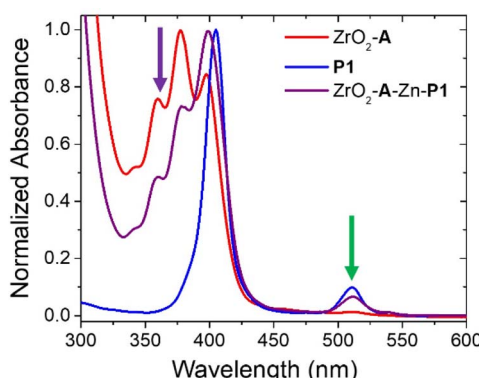


Fig. 2 Absorption spectra of $\text{ZrO}_2\text{-A}$, $\text{ZrO}_2\text{-A-Zn-P1}$, and **P1** in chloroform:methanol (1 : 1, v/v). Purple and green arrows indicate 360 and 512 nm excitation wavelengths, respectively.

Excited state energy transfer

${}^1\text{A}^*$ to **PX** energy transfer was first probed using time-resolved emission spectroscopy (TRES) and the results are shown in Fig. 3. Under 360 nm excitation, emission features from $\text{ZrO}_2\text{-A}$ are consistent with fluorescent decay from the ${}^1\text{A}^*$ state,³² whose kinetics at 460 nm could be fit with a biexponential function. The amplitude (A_x) and lifetime (τ_x) for each component as well as the weighted average lifetime ($\tau_{w(A)}$) are summarized in Table S1.[†] Multiexponential fitting of even a single surface bound emitter is common and is often attributed to inhomogeneous local environments in the film.^{32,51} Nonetheless, the weighted average lifetime of 5 ns is reasonably consistent with that observed in solution.⁴⁰

In the $\text{ZrO}_2\text{-A-Zn-PX}$ films, following preferential excitation of **A** at 360 nm, **A** emission is quenched with the decay rate increasing in the order of **P3** < **P2** ≈ **P1** (Fig. 3). This observation is consistent with excited state quenching of **A** *via* ${}^1\text{A}^*$ to **PX** Förster Resonance Energy Transfer (FRET), whose efficiency decreases as the number of phenylene spacers increases (X in Fig. 1). The excited state decay for **P1**- and **P2**-containing films were near our instrument response function ($\text{IRF} \approx 1$ ns) but decay kinetics from the $\text{ZrO}_2\text{-A-Zn-P3}$ films were fit using IRF deconvolution, giving a weighted average lifetime of 3.1 ± 0.3 ns.

Assuming that energy transfer to **P3** is the only additional quenching mechanism introduced in the bilayer, then the rate constant for energy transfer (k_{FRET}) can be estimated using eqn (4):

$$k_{\text{FRET}} = \frac{1}{\tau_{\text{bl}}} - \frac{1}{\tau_A} \quad (4)$$

where τ_A and τ_{bl} are the weighted average lifetime for anthracene emission in the $\text{ZrO}_2\text{-A}$, and $\text{ZrO}_2\text{-A-Zn-P3}$ films, respectively.³² However, the calculated rate constant of $1.0 \pm 0.4 \times 10^8$ s^{-1} is a low end estimate of k_{FRET} because (1) this measurement only captures kinetics after 1 ns and (2) not all **A** molecules are necessarily involved in the energy transfer process resulting in contributions from the intrinsic emission decay of ${}^1\text{A}^*$.⁴¹

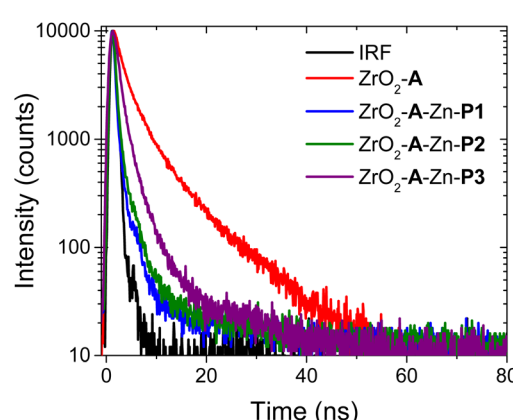


Fig. 3 Time-resolved emission at 460 nm for $\text{ZrO}_2\text{-A}$ and $\text{ZrO}_2\text{-A-Zn-PX}$ in MeCN ($\lambda_{\text{ex}} = 360$ nm).



To circumvent these limitations, we performed ultrafast transient absorption (TA) spectroscopy, and the results are shown in Fig. 4 with the kinetic fits summarized in Table S2.† For the $\text{ZrO}_2\text{-A}$ film excited at 360 nm, there is a prominent excited state absorption (ESA) feature at 575 nm that decays in ~ 2 ns, in line with ${}^1\text{A}^*$ emission described above. Upon excitation with 512 nm, $\text{ZrO}_2\text{-P1}$ exhibits a ground state bleach for the Q-band at ~ 515 nm and broad excited state absorption from 400–800 nm. These features persist well beyond the instrument time resolution of 7 ns and are in agreement with rapid inter-system crossing followed by excited state decay from the triplet state of **P1** (${}^3\text{P1}^*$).^{41,52,53}

Under 360 nm excitation of **A**, all three bilayer films are initially dominated by the ESA of ${}^1\text{A}^*$ followed by the appearance of ${}^3\text{PX}^*$ features. The late time contribution of ${}^3\text{PX}^*$ is notably lower in the $\text{ZrO}_2\text{-A-Zn-P3}$ film, where energy transfer is expected to be slower and less efficient. The kinetics for the growth of **PX** excited states were monitored at 460 nm (*i.e.*, the isosbestic point for $\text{ZrO}_2\text{-A}$) and the results are shown in Fig. 4c. For all three films, there is a growth of ${}^3\text{PX}^*$ ESA that largely plateaus by 400 ps and persists beyond 7 ns. This is in contrast to the instrument limited ESA observed at 460 nm for $\text{ZrO}_2\text{-P1}$ following direct excitation of **P1** at 512 nm (blue in Fig. 4c). We attribute the slow growth of ${}^3\text{PX}^*$ features in the $\text{ZrO}_2\text{-A-Zn-PX}$ films to a mechanism consisting of excitation of **A**, ${}^1\text{A}^*$ to **PX** FRET, rapid inter-system crossing from ${}^1\text{PX}^*$ to ${}^3\text{PX}^*$, followed by slow excited state decay from ${}^3\text{PX}^*$. It is important to note that our previous surface dilution studies indicate that the rapid energy transfer in the $\text{ZrO}_2\text{-A-Zn-P3}$ film is dominated by inter-assembly energy transfer (*i.e.*, between metal ion linked molecules) and not inter-layer energy transfer (*i.e.*, between non-

linked molecules in separate layers).⁴¹ Consequently, the energy transfer dynamics measured here are likely dictated by the relative structure of the molecules within the metal ion linked assemblies.

The weighted average lifetime and rate constant for the appearance of ${}^3\text{PX}^*$ (*i.e.*, k_{FRET}) in $\text{ZrO}_2\text{-A-Zn-PX}$ were obtained from a biexponential fit and the data are summarized in Table S2.† The k_{FRET} increases in the order **P3** ($0.6 \times 10^{10} \text{ s}^{-1}$) $<$ **P2** ($2.4 \times 10^{10} \text{ s}^{-1}$) \approx **P1** ($2.4 \times 10^{10} \text{ s}^{-1}$). The trend again reveals an expected decrease in k_{FRET} with increasing distance (r_{DA} in eqn (1)) between the donor (**A**) and acceptor (**PX**). While the trend is generally reproducible across several sets of samples, it is important to acknowledge that the lifetime for **P1** and **P2** are similar within measurement standard deviation. Furthermore, the difference in k_{FRET} between $\text{ZrO}_2\text{-A-Zn-P1}$ and $\text{ZrO}_2\text{-A-Zn-P2}$ is smaller than one might expect for an r_{DA}^6 distance dependence. This observation suggests that distance is not the only FRET relevant parameter changing between the two samples, and that the relative orientation of the chromophores in the assembly may also change due to the presence of an additional phenylene spacer.

As an aside, we also investigated the ${}^3\text{PX}^*$ to **A** triplet energy transfer (TET) using time-resolved emission from ${}^3\text{PX}^*$ and the results are summarized in Fig. S7 and Table S3.† Consistent with the results above, the TET energy transfer rate for $\text{ZrO}_2\text{-A-Zn-PX}$ increases in the order of **P3** ($4.5 \times 10^3 \text{ s}^{-1}$) $<$ **P2** ($7.0 \times 10^3 \text{ s}^{-1}$) $<$ **P1** ($9.8 \times 10^3 \text{ s}^{-1}$). This also agrees with the expectation of slowed TET with increasing r_{DA} .⁵⁴ Worth noting is that the necessity of orbital overlap for electron transfer suggests TET could also exhibit an orientation dependence^{55–57} but experimental support for such phenomenon is limited.

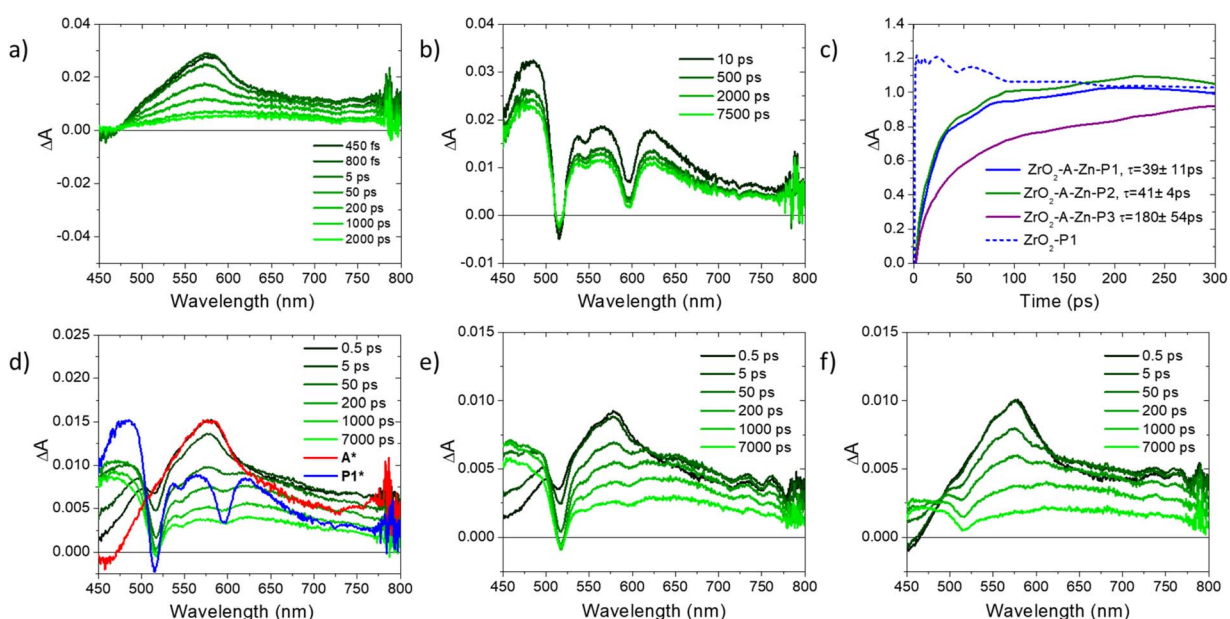


Fig. 4 Transient absorption spectra for (a) $\text{ZrO}_2\text{-A}$ ($\lambda_{\text{ex}} = 360$ nm) and (b) $\text{ZrO}_2\text{-P1}$ ($\lambda_{\text{ex}} = 512$ nm). (c) Single wavelength kinetics for $\text{ZrO}_2\text{-A-Zn-PX}$ at 460 nm ($\lambda_{\text{ex}} = 360$ nm) and $\text{ZrO}_2\text{-P1}$ at 460 nm ($\lambda_{\text{ex}} = 512$ nm). Transient absorption spectra for $\text{ZrO}_2\text{-A-Zn-PX}$ where (d) $X = 1$, (e) $X = 2$, and (f) $X = 3$ ($\lambda_{\text{ex}} = 360$ nm). Red and blue overlays in (d) are spectra at 500 fs for $\text{ZrO}_2\text{-A}$ and 10 ps $\text{ZrO}_2\text{-P1}$, respectively. All samples were measured in nitrogen deaerated MeCN.



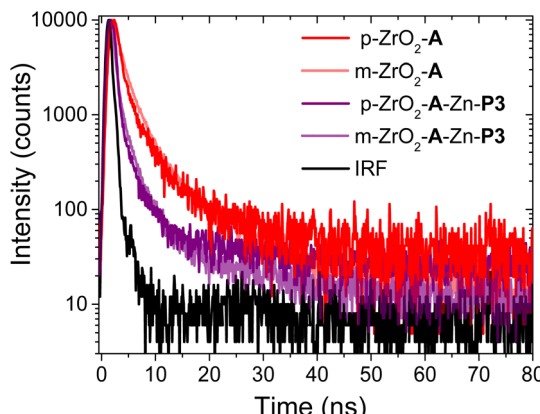


Fig. 5 Time-resolved emission decays at 460 nm for planar (p-) and mesoporous (m-) $\text{ZrO}_2\text{-A}$ and $\text{ZrO}_2\text{-A-Zn-P3}$ in MeCN ($\lambda_{\text{ex}} = 360$ nm).

Planar vs. mesoporous substrates

Spectroscopic measurements, like those in the previous section, as well as light harvesting/generating applications of molecule–metal oxide interfaces typically rely on mesoporous, fused nanoparticle substrates. This choice is due to their high surface areas, enabling increased absorption cross-section and amplified signals.²⁹ In contrast, a majority of techniques used to determine the structure of molecule–metal oxide interfaces, including those discussed below, are performed on planar substrates.^{20,58,59} The underlying, but untested assumption is that the structure at the molecule–metal oxide interface is the same on planar (p-) and mesoporous (m-) substrates. Here we use **A** to **P3** FRET in the **A-Zn-P3** bilayer as an indirect probe of the interfacial structure on planar and mesoporous ZrO_2 . Due to the inherent technical challenges of performing TA on planar substrates (*i.e.*, low absorption and ΔA), we relied on time-resolved emission of the $\text{ZrO}_2\text{-A-Zn-P3}$ bilayer, where k_{FRET} was sufficiently slowed and resolvable by our TCSPC emission measurement.

Following 360 nm excitation, ${}^1\text{A}^*$ emission decay kinetics for **A** and **A-Zn-P3** films on p- ZrO_2 and m- ZrO_2 were measured, and the results are shown in Fig. 5 with kinetic fitting parameters summarized in Table S4.[†] Both substrates exhibit similar kinetics for both the monolayer and bilayer films. From the fits to the data, the average lifetimes, and eqn (4), similar k_{FRET} of $1.3 \pm 0.1 \times 10^8 \text{ s}^{-1}$ and $1.0 \pm 0.4 \times 10^8 \text{ s}^{-1}$ were determined for bilayers on p- ZrO_2 and m- ZrO_2 , respectively. Given that each film has the same solvent (n) and chromophore pair (*i.e.*, constant J and Φ_D), this observation suggests that r_{DA} and κ^2 are similar for the **A** and **P3** pair, regardless of the nature of the underlying substrate. This data strongly suggests that the structure of the bilayer film is similar on both planar and mesoporous substrates and that structural measurements on a planar surface (*vide infra*) can serve as a reasonable surrogate for mesoporous films.

Polarized attenuated total reflectance

Insights into the structure of the $\text{ZrO}_2\text{-A-Zn-PX}$ bilayers were obtained using polarized UV-Vis attenuated total reflectance

spectroscopy (p-ATR).^{31,60–62} p-ATR is performed by binding the molecule to a metal oxide coated glass waveguide that enables multiple internal reflections at the metal oxide–molecule–solvent interface. Then, the difference in attenuated absorption between transverse electric and transverse magnetic UV-Vis light can be used to determine the mean tilt angles of the transition dipole moment (θ_{tilt}) of chromophores relative to the surface normal. ITO, as opposed to ZrO_2 (*vide supra*), was used as the metal oxide substrate because highly planar films on waveguiding glass slides (*i.e.*, RMS surface roughness of $0.5 \pm 0.1 \text{ nm}$) are commercially available.^{23,25} Importantly, our recent study shows that at high surface coverage, the orientation of molecules is similar regardless of the nature of the metal oxide (*e.g.*, ITO, TiO_2 , ZrO_2) indicating that ITO can serve as a reasonable surrogate for ZrO_2 .²³

p-ATR was used to monitor the multilayer assembly process and measure the surface coverage and θ_{tilt} of the chromophore films. Results are summarized in Table 1 with additional data and experimental data/details provided in the ESI.[†] Consistent with previous reports,^{23–25} the **A** films achieve a hexagonal closest packed surface loading of $\sim 3 \times 10^{-10} \text{ mol cm}^{-2}$ and a tilt angle of $\sim 30^\circ$, which slightly increases with Zn ($\sim 35^\circ$), and **PX** ($\sim 37^\circ$) coordination. **P1-3** loaded on the ITO-A-Zn with a surface coverage of $\sim 3 \times 10^{-11} \text{ mol cm}^{-2}$, resulting in an $\sim 10:1$, **A**:**PX** loading ratio as observed on m- ZrO_2 . Interestingly, the tilt angle of the porphyrin (*i.e.*, the plane of the porphyrin core) relative to surface normal increases in the order of **P3** (22°) $<$ **P2** (36°) $<$ **P1** (50°) in the ITO-A-Zn-PX films.

Based on the p-ATR data, a depiction of the molecular orientations relative to the ITO surface normal for ITO-A-Zn-PX films are shown in Fig. 6. To generate these drawings, the tilt angle for **A** is depicted using the transition dipole across the 9,10-carbon atoms of the anthracene^{43,63} and for **PX**, the plane of the porphyrin core is used and assumed to be aligned with the axis of the phenylene carboxylate linker.^{49,64}

While some structural insights were obtained from this measurement, two critical points must be made. First, even in the absence of an exact structure, the porphyrin plane angle changes among the three bilayers. Consequently, κ^2 is not equivalent, so the number of phenylene spacers (*i.e.*, r_{DA}) and FRET efficiency cannot be used to determine the relative orientation between the chromophores uniformly across the series. Second, for a chromophore with a linear transition

Table 1 Surface coverages and mean tilt angle (θ_{tilt}) of **A**, **A-Zn**, and **A-Zn-PX** adsorbed on ITO as determined from p-ATR^a

Film on ITO	θ_{tilt} ($^\circ$)	Surface coverage (mol cm^{-2})
A	30 ± 1^b	$3.1 \pm 0.2 \times 10^{-10}^b$
A in (A-Zn)	35 ± 3^b	
A in (A-Zn-P1)	37 ± 3^b	
P1 in (A-Zn-P1)	50 ± 1	$2.8 \pm 0.9 \times 10^{-11}$
P2 in (A-Zn-P2)	36 ± 2	$5 \pm 2 \times 10^{-11}$
P3 in (A-Zn-P3)	22 ± 4	$3 \pm 2 \times 10^{-11}$

^a For all cases, $n = 3$ trials and the error is the standard deviation of the three trials. ^b Results from the **A-Zn-P1** bilayer. A surface coverage and θ_{tilt} data from the **A-Zn-P2** and **A-Zn-P3** bilayers are provided in the ESI.



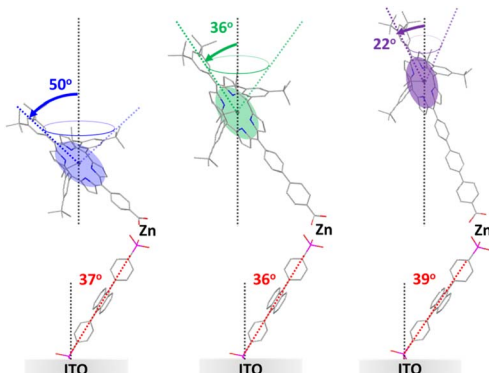


Fig. 6 Schematic representation of the mean polar tilt angles for A and PX in A-Zn-P1 (left), A-Zn-P2 (middle), and A-Zn-P3 (right) on ITO. Cones represent possible porphyrin orientations assuming the plane of the porphyrin is aligned with the axis of the phenylene carboxylate linker.

dipole moment, a cone is sufficient to capture all possible angles of the second layer chromophore relative to the surface normal and first chromophore. However, as we will discuss in the next section, the circularly polarized transition plane of the porphyrin greatly expands the range of possible structures.

FRET efficiency and structure

As noted above, p-ATR only provides information about the orientation of the porphyrin plane relative to the surface normal. Therefore, even the cone angle depicted in Fig. 6 is insufficient to capture all possible orientations of the porphyrin plane. To explore possible structures, we performed geometric calculations with key structural parameters shown in Fig. 7 (see ESI† for details). The model consists of vector representations for A and PX in red and purple, respectively (Fig. 7a), arranged in all possible relative orientations (Fig. 7b), onto which vector representations of the transition dipoles were then superimposed (Fig. S15†). This analysis was performed in three steps: (1) establishing a full set of possible geometries where the transition dipole vectors of A and PX agree with the angles determined by p-ATR, (2) calculating the FRET efficiency for each of the geometries using eqn (1)–(3), and (3) comparing calculated and experimental efficiencies to determine the most probable orientation.

To begin, we assume that A is oriented at a fixed angle (θ_A) relative to the surface normal, as determined by p-ATR, and that the Zn-ion acts as a stationary vertex around which PX can freely rotate. In our model, the Zn linker ion is set as the origin of coordinates, surface normal is set as the z-axis, and the vector representation of A (r_A) is set in the x,z-plane. The free motion of the vector model for PX (r_P) consists of azimuthal (φ) and altitudinal (θ_P) rotations, giving a theoretical sphere which r_P can trace (Fig. 7b). Additionally, free rotation of the porphyrin plane about the meso-axis (θ_{rot}) allows PX to adopt geometries outside of the cone depicted in Fig. 6. Given the constraint that the maximum gradient of the porphyrin plane must be at the angle θ_{tilt} from surface normal, the set of possible orientations for PX is restricted to a spherical frustum shown in Fig. S15.†

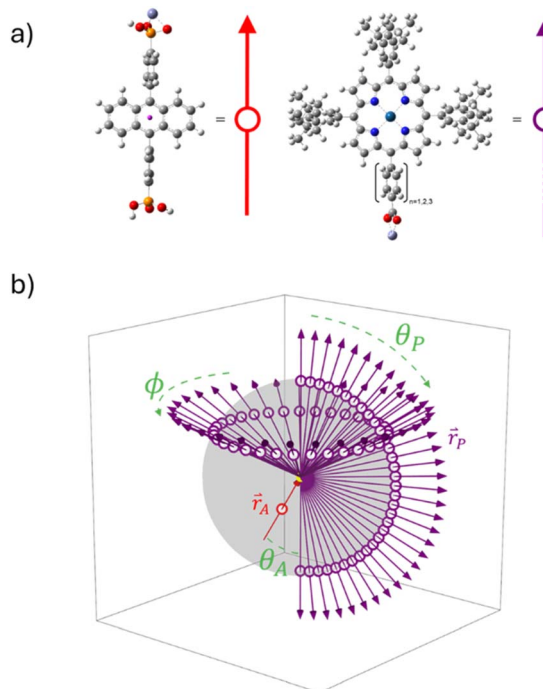


Fig. 7 (a) Vector representations of the transition dipole moments of A (red) and PX (purple) with the chromophore centroid depicted as a circle. (b) Geometric orientation of vectors showing permutation by altitudinal (θ_P) and azimuthal (φ) rotation. In this model space, θ_P is defined as the angle to the positive z-axis and φ is defined as the angle between the projection of r_P onto the x,y-plane and the positive x-axis.

Using eqn (1) and (2) with κ^2 and r_{DA} from the model structures, as well as $J = 2 \times 10^{-14}$, $\Phi_D = 0.53$, and $n = 1.36$ from experimental values^{40,65} we calculated theoretical FRET efficiencies (E_{theo}) for all of the geometries and the results are shown in Fig. 8a, S16a and b.† In line with prior literature,⁶⁶ for these calculations we used the average κ^2 from two perpendicular, degenerate transition dipole moments of the porphyrin plane (*i.e.*, one aligned with the long axis and one perpendicular through the orthogonal meso-carbons).

The surfaces of E_{theo} for the A-Zn-PX models generally look similar (Fig. S16a–c†) but with differences in amplitude of E_{theo} . Particularly notable is that in the case of P1, the short r_{DA} leads to high E_{theo} (>0.99) across a majority of the surface (Fig. S16a†). In contrast, a larger variation in E_{theo} is observed for the bilayer containing P2 (Fig. S16b†) and P3 (Fig. 8a).

To determine the geometries that are most consistent with the experimentally determined FRET efficiencies (E_{exp}), we constructed heatmaps showing the absolute difference between E_{theo} and E_{exp} (Fig. S16g–i†). For these heatmaps, E_{exp} was calculated using eqn (5)

$$E_{\text{exp}} = \frac{\frac{k_{\text{FRET}}}{k_{\text{r}} + k_{\text{nr}}}}{1 - \frac{k_{\text{FRET}}}{k_{\text{r}} + k_{\text{nr}}}} \quad (5)$$

where k_{FRET} is the FRET rate constant for each $\text{ZrO}_2\text{-A-Zn-PX}$ film (*vide supra*), and k_{r} ($8.8 \times 10^7 \text{ s}^{-1}$) and k_{nr} ($7.8 \times 10^7 \text{ s}^{-1}$) are



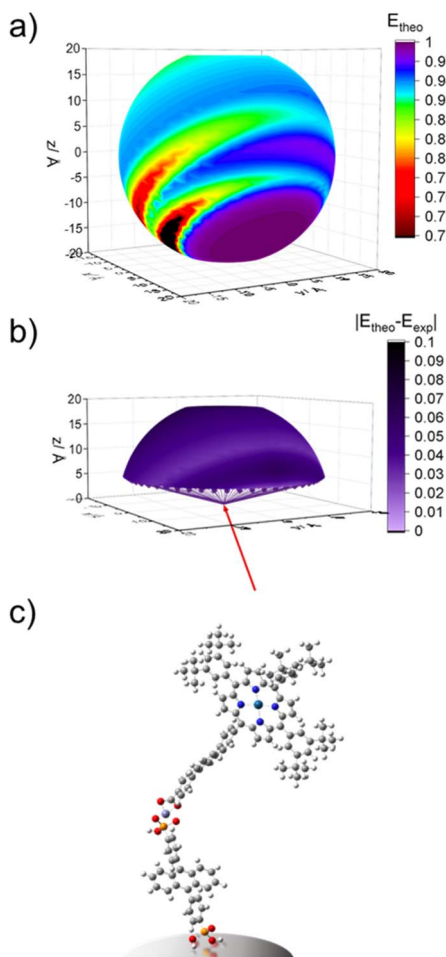


Fig. 8 (a) Calculated A to P3 FRET efficiencies for $\text{ZrO}_2\text{-A-Zn-P3}$ where θ_A is 39° and P3 is oriented at all geometries with a porphyrin core plane angle of 22° relative to surface normal. (b) Heatmap depicting absolute difference between theoretical and experimental FRET efficiencies. (c) Example geometry of a bilayer orientation within the feasible band ($\theta_P = 53^\circ$, $\varphi = 21^\circ$, $\theta_{\text{rot}} = 62^\circ$).

the intrinsic radiative and non-radiative rate constants, respectively, for **PX**. From this equation we obtain an energy transfer efficiency of 0.99, 0.99, and 0.97 for bilayers containing **P1**, **P2**, and **P3**, respectively. Note that because k_{FRET} was determined from the ultrafast TA measurements, it only captures dynamics/yields of intra-assembly energy transfer,⁴¹ and in-turn structural aspects of the metal ion linked donor-acceptor pair.

The heatmaps for $|E_{\text{theo}} - E_{\text{exp}}|$ were then projected onto the spherical sections and the results are shown in Fig. 8b and S16g-i.[†] The lower portions of the spheres were omitted ($x < 5 \text{ \AA}$) because it is assumed that due to steric constraints, **PX** is unable to adopt geometries that would place the 3,5-di-*tert*-butylbenzene groups deep within the $\text{ZrO}_2\text{-A-Zn}$ sublayers.

For the **A-Zn-P1** bilayer, there is a broad range of possible geometries that show agreement between calculated and experimental values ($|E_{\text{theo}} - E_{\text{exp}}| < 0.01$). In contrast, for bilayers containing **P2** (Fig. S16h[†]) and **P3** (Fig. 8b), there is an apparent radial band across the sphere indicating that those

structures exhibit stronger agreement between E_{theo} and E_{exp} . Among the possible geometries we selected example structures that show the best theoretical-experimental agreement, and those structures are depicted in Fig. 8c for $\text{ZrO}_2\text{-A-Zn-P3}$ with the remaining structures in Fig. S16.[†]

Conclusions

Here we prepare metal ion-linked bilayer films containing a series of platinum porphyrin derivatives with one (**P1**), two (**P2**), or three (**P3**) phenylene spacers between the chromophoric core and the metal ion binding carboxylate group. The porphyrins were bound to a phosphonated anthracene (**A**) functionalized mesoporous ZrO_2 surface with a $\text{Zn}(\text{II})$ linking ion to generate the $\text{ZrO}_2\text{-A-Zn-PX}$ bilayer films. Both time-resolved emission and transient absorption measurements indicate that the rate and efficiency of A^* to **PX** FRET generally decrease in the order of $\text{P1} \geq \text{P2} > \text{P3}$. With the FRET efficiency in hand, our goal was to use known parameters in the FRET equation (*i.e.*, overlap integral, refractive index, and fluorescence quantum yield of the donor), combined with a systematic change in r_{DA} with phenylene spacer length, to calculate the orientation factor (κ^2) across the series. This method assumes that κ^2 is the same for all three bilayers. However, UV-Vis polarized visible attenuated total reflectance (p-ATR) indicate that the tilt angle of the porphyrin relative to surface normal increases in the order of **P3** (22°) < **P2** (36°) < **P1** (50°). Consequently, the interchromophore distance and orientation are changing with each bilayer and thus the method described above cannot be used to determine κ^2 across the series.

Furthermore, p-ATR only provides information regarding the orientation of the porphyrin plane relative to the surface normal which greatly expands the possible orientations of the long axis of the molecule relative to **A**. To narrow the scope of possible structures, we performed geometric calculations of all possible structures that agree with the angles determined by p-ATR and determined the theoretical FRET efficiency of each geometry. Then by comparing calculated and experimental efficiencies we proposed the most likely structures of the bilayer films.

Additionally, we compared the energy transfer rate of **A-Zn-P3** bilayers on mesoporous and planar ZrO_2 substrates. The nearly identical energy transfer rate indicates that the structure of the bilayer is similar, regardless of the nature of the underlying substrate. This observation is critical in that, after decades of assuming the structures are the same, this report provides strong evidence that the structure is consistent on planar and mesoporous substrates, and each can serve as a reasonable surrogate for the other.

In summary, while we were unable to determine an absolute structure, this work provides new structural insights into multilayer films on planar and mesoporous surfaces. Additionally, we demonstrate the promise of p-ATR and FRET as complementary techniques to determine the structure of multichromophore assemblies. Going forward, the use of an acceptor chromophore with a linear transition dipole moment (*i.e.*, not a porphyrin) will dramatically narrow the possible range of structures and will enable the determination of

a single, likely structure of the bilayer assembly. Furthermore, with these tools in hand, we look forward to investigating the role of variables like metal ion binding motif, surface coverage, linking metal ion, *etc.* in dictating the structure of these multilayer assemblies. With increased insights, one can envision controlling such structures to design assemblies that facilitate or hinder energy and electron transfer processes, for example, as desired for a given application.

Data availability

The data supporting this article have been included as part of the ESI.†

Conflicts of interest

There are no conflicts to declare.

Acknowledgements

Energy transfer measurements were supported by the National Science Foundation under Grant No. DMR-2327754. Characterization of the bilayer formation was supported by the Army Research Office under Grant No. W911NF-19-1-0357. A. I. is grateful to the National Science Foundation (CHE-2102579) for the support of fundamental research. A. A. acknowledges the Arnold O. Beckman Postdoctoral Fellowship Program. C. R. acknowledges support from Fonds de recherche du Québec – Nature et technologies scholarships. Some of the ATR data were acquired in the W. M. Keck Center for Nano-Scale Imaging in the Department of Chemistry and Biochemistry at the University of Arizona. This instrument was supported as part of the Center for Interface Science: Solar-Electric Materials (CIS: SEM), an Energy Frontier Research Center funded by the U.S. Department of Energy, Office of Science, Office of Basic Energy Sciences under Award No. DE-SC0001084.

References

- 1 S. P. Pujari, L. Scheres, A. T. M. Marcelis and H. Zuilhof, *Angew. Chem., Int. Ed.*, 2014, **53**, 6322–6356.
- 2 E. Galoppini, *Coord. Chem. Rev.*, 2004, **248**, 1283–1297.
- 3 A. Arcidiacono, B. Hanks and K. Hanson, *ACS Appl. Opt. Mater.*, 2023, **1**, 1156–1168.
- 4 J. C. Wang, S. P. Hill, T. Dilbeck, O. O. Ogunsolu, T. Banerjee and K. Hanson, *Chem. Soc. Rev.*, 2018, **47**, 104–148.
- 5 Y. Zhou, C. Ruchlin, A. J. Robb and K. Hanson, *ACS Energy Lett.*, 2019, **4**, 1458–1463.
- 6 S. P. Hill, T. Dilbeck, E. Baduell and K. Hanson, *ACS Energy Lett.*, 2016, **1**, 3–8.
- 7 D. Beery, T. W. Schmidt and K. Hanson, *ACS Appl. Mater. Interfaces*, 2021, **13**, 32601–32605.
- 8 O. O. Ogunsolu, I. A. Murphy, J. C. Wang, A. Das and K. Hanson, *ACS Appl. Mater. Interfaces*, 2016, **8**, 28633–28640.
- 9 X. Ding, Y. Gao, L. Zhang, Z. Yu, J. Liu and L. Sun, *ACS Catal.*, 2014, **4**, 2347–2350.
- 10 N. Yoshimura, M. Yoshida, M. Kato and A. Kobayashi, *Inorg. Chem.*, 2022, **61**, 11095–11102.
- 11 M. A. Gross, C. E. Creissen, K. L. Orchard and E. Reisner, *Chem. Sci.*, 2016, **7**, 5537–5546.
- 12 O. O. Ogunsolu, J. C. Wang and K. Hanson, *ACS Appl. Mater. Interfaces*, 2015, **7**, 27730–27734.
- 13 J. C. Wang, I. A. Murphy and K. Hanson, *J. Phys. Chem. C*, 2015, **119**, 3502–3508.
- 14 B. H. Farnum, K.-R. Wee and T. J. Meyer, *Nat. Chem.*, 2016, **8**, 845–852.
- 15 R. N. Sampaio, L. Troian-Gautier and G. J. Meyer, *Angew. Chem.*, 2018, **130**, 15616–15620.
- 16 Z.-J. Li, C.-J. Yao and Y.-W. Zhong, *Sci. China: Chem.*, 2019, **62**, 1675–1685.
- 17 A. Arcidiacono, A. J. Robb, R. A. Masitas, S. R. Salpage, G. M. McLeod, J. Chen, O. O. Ogunsolu, M. G. Roper and K. Hanson, *J. Photochem. Photobiol.*, 2022, **9**, 100088.
- 18 K. Hanson, D. A. Torelli, A. K. Vannucci, M. K. Brenneman, H. Luo, L. Alibabaei, W. Song, D. L. Ashford, M. R. Norris, C. R. K. Glasson, J. J. Concepcion and T. J. Meyer, *Angew. Chem., Int. Ed.*, 2012, **51**, 12782–12785.
- 19 A. J. Robb, D. Miles, S. R. Salpage, N. Watson, Q. He, Q. Wu and K. Hanson, *ACS Appl. Mater. Interfaces*, 2020, **12**, 38003–38011.
- 20 B. Tosco, B. P.-A. V. Melo, D. Hermida Merino, J. F. Q. Rey and S. Brochsztajn, *Langmuir*, 2021, **37**, 2494–2502.
- 21 H. C. Yang, K. Aoki, H. G. Hong, D. D. Sackett, M. F. Arendt, S. L. Yau, C. M. Bell and T. E. Mallouk, *J. Am. Chem. Soc.*, 1993, **115**, 11855–11862.
- 22 H. Byrd, J. L. Snover and M. E. Thompson, *Langmuir*, 1995, **11**, 4449–4453.
- 23 D. Pattadar, L. Zheng, A. J. Robb, D. Beery, W. Yang, K. Hanson and S. S. Saavedra, *J. Phys. Chem. C*, 2023, **127**, 2705–2715.
- 24 A. Arcidiacono, Y. Zhou, W. Zhang, J. O. Ellison, S. Ayad, E. S. Knorr, A. N. Peters, L. Zheng, W. Yang, S. S. Saavedra and K. Hanson, *J. Phys. Chem. C*, 2020, **124**, 23597–23610.
- 25 D. Pattadar, A. Arcidiacono, D. Beery, K. Hanson and S. S. Saavedra, *Langmuir*, 2023, **39**, 10670–10679.
- 26 M. J. Griffith, M. James, G. Triani, P. Wagner, G. G. Wallace and D. L. Officer, *Langmuir*, 2011, **27**, 12944–12950.
- 27 M. Gliboff, L. Sang, K. M. Knesting, M. C. Schalnat, A. Mudalige, E. L. Ratcliff, H. Li, A. K. Sigdel, A. J. Giordano, J. J. Berry, D. Nordlund, G. T. Seidler, J.-L. Brédas, S. R. Marder, J. E. Pemberton and D. S. Ginger, *Langmuir*, 2013, **29**, 2166–2174.
- 28 L. Sang, A. Mudalige, A. K. Sigdel, A. J. Giordano, S. R. Marder, J. J. Berry and J. E. Pemberton, *Langmuir*, 2015, **31**, 5603–5613.
- 29 A. J. Robb, E. S. Knorr, N. Watson and K. Hanson, *J. Photochem. Photobiol. A*, 2020, **390**, 112291.
- 30 W. J. Doherty, C. L. Donley, N. R. Armstrong and S. S. Saavedra, *Appl. Spectrosc.*, 2002, **56**, 920–927.
- 31 S. B. Mendes, J. T. Bradshaw and S. S. Saavedra, *Appl. Opt.*, 2004, **43**, 70–78.
- 32 T. Dilbeck, J. C. Wang, Y. Zhou, A. Olsson, M. Sykora and K. Hanson, *J. Phys. Chem. C*, 2017, **121**, 19690–19698.



33 Y. Zhou, S. Ayad, C. Ruchlin, V. Posey, S. P. Hill, Q. Wu and K. Hanson, *Phys. Chem. Chem. Phys.*, 2018, **20**, 20513–20524.

34 L. Stryer and R. P. Haugland, *Proc. Natl. Acad. Sci. U. S. A.*, 1967, **58**, 719–726.

35 Th. Förster, *Ann. Phys.*, 1948, **437**, 55–75.

36 J. R. Lakowicz, *Principles of Fluorescence Spectroscopy*, Springer Science & Business Media, 2013.

37 V. Gray, B. Küçüköz, F. Edhborg, M. Abrahamsson, K. Moth-Poulsen and B. Albinsson, *Phys. Chem. Chem. Phys.*, 2018, **20**, 7549–7558.

38 V. Gray, K. Börjesson, D. Dzebo, M. Abrahamsson, B. Albinsson and K. Moth-Poulsen, *J. Phys. Chem. C*, 2016, **120**, 19018–19026.

39 S.-H. A. Lee, N. M. Abrams, P. G. Hoertz, G. D. Barber, L. I. Halaoui and T. E. Mallouk, *J. Phys. Chem. B*, 2008, **112**, 14415–14421.

40 S. P. Hill, T. Banerjee, T. Dilbeck and K. Hanson, *J. Phys. Chem. Lett.*, 2015, **6**, 4510–4517.

41 G. M. McLeod, J. Nolder, A. Arcidiacono, S. Lindbom, N. Dos Santos, E. Lambert, S. Ayad, D. Beery, I. Alabugin and K. Hanson, *J. Phys. Chem. C*, 2024, DOI: [10.1021/acs.jpcc.4c04033](https://doi.org/10.1021/acs.jpcc.4c04033).

42 Y. Zheng, A. J. Giordano, R. C. Shallcross, S. R. Fleming, S. Barlow, N. R. Armstrong, S. R. Marder and S. S. Saavedra, *J. Phys. Chem. C*, 2016, **120**, 20040–20048.

43 B. Norden, G. Lindblom and I. Jonas, *J. Phys. Chem.*, 1977, **81**, 2086–2093.

44 S. P. Hill and K. Hanson, *J. Am. Chem. Soc.*, 2017, **139**, 10988–10991.

45 P. Bharmoria, H. Bildirir and K. Moth-Poulsen, *Chem. Soc. Rev.*, 2020, **49**, 6529–6554.

46 Y. Zhou, S. P. Hill and K. Hanson, *J. Photonics Energy*, 2017, **8**, 022004.

47 J. S. Lindsey, *Acc. Chem. Res.*, 2010, **43**, 300–311.

48 P. Mishra, J. P. Hill, S. Vijayaraghavan, W. V. Rossom, S. Yoshizawa, M. Grisolia, J. Echeverria, T. Ono, K. Ariga, T. Nakayama, C. Joachim and T. Uchihashi, *Nano Lett.*, 2015, **15**, 4793–4798.

49 M. Gouterman, *J. Mol. Spectrosc.*, 1961, **6**, 138–163.

50 R. Katoh, A. Furube, T. Yoshihara, K. Hara, G. Fujihashi, S. Takano, S. Murata, H. Arakawa and M. Tachiya, *J. Phys. Chem. B*, 2004, **108**, 4818–4822.

51 J. R. Durrant, S. A. Haque and E. Palomares, *Coord. Chem. Rev.*, 2004, **248**, 1247–1257.

52 Y. Venkatesh, M. Venkatesan, B. Ramakrishna and P. R. Bangal, *J. Phys. Chem. B*, 2016, **120**, 9410–9421.

53 S. M. Aly, S. Goswami, Q. A. Alsulami, K. S. Schanze and O. F. Mohammed, *J. Phys. Chem. Lett.*, 2014, **5**, 3386–3390.

54 D. L. Dexter, *J. Chem. Phys.*, 1953, **21**, 836–850.

55 H. S. Judeikis and S. Siegel, *J. Chem. Phys.*, 1970, **53**, 3500–3506.

56 J. K. Roy and M. A. El-Sayed, *J. Chem. Phys.*, 1964, **40**, 3442–3443.

57 K. B. Eisenthal, *J. Chem. Phys.*, 1969, **50**, 3120–3122.

58 V. Kaliginedi, H. Ozawa, A. Kuzume, S. Maharajan, I. V. Pobelov, N. Hee Kwon, M. Mohos, P. Broekmann, K. M. Fromm, M. Haga and T. Wandlowski, *Nanoscale*, 2015, **7**, 17685–17692.

59 H. E. Katz, W. L. Wilson and G. Scheller, *J. Am. Chem. Soc.*, 1994, **116**, 6636–6640.

60 L. E. Oquendo, R. Ehamparam, N. R. Armstrong, S. S. Saavedra and D. V. McGrath, *J. Phys. Chem. C*, 2019, **123**, 6970–6980.

61 R. Ehamparam, L. E. Oquendo, M. W. Liao, A. K. Brynnel, K.-L. Ou, N. R. Armstrong, D. V. McGrath and S. S. Saavedra, *ACS Appl. Mater. Interfaces*, 2017, **9**, 29213–29223.

62 P. L. Edmiston, J. E. Lee, S.-S. Cheng and S. S. Saavedra, *J. Am. Chem. Soc.*, 1997, **119**, 560–570.

63 H. Inoue, T. Hoshi, T. Masamoto, J. Shiraishi and Y. Tanizaki, *Ber. Bunsenges. Phys. Chem.*, 1971, **75**, 441–446.

64 J. A. Shelnutt and V. Ortiz, *J. Phys. Chem.*, 1985, **89**, 4733–4739.

65 S. S. Saavedra and W. M. Reichert, *Anal. Chem.*, 1990, **62**, 2251–2256.

66 J. Mårtensson, *Chem. Phys. Lett.*, 1994, **229**, 449–456.

